Check for updates

IET Nanodielectrics

WILEY

The Institution of Engineering and Technology

ORIGINAL RESEARCH OPEN ACCESS

Enhancing Electrospun PVDF-HFP Nanofibres for Lithium-Ion Battery Separators Through the Incorporation of Inorganic Nanoparticles: Physico-Chemical and Electrical Characterisation

Leonardo Gasperini | Iacopo Iannarelli | Simone Vincenzo Suraci | Davide Fabiani

LIMES, Department of Electrical, Electronic, and Information Engineering, Guglielmo Marconi, University of Bologna, Bologna, Italy

Correspondence: Leonardo Gasperini (leonardo.gasperini@unibo.it)

Received: 23 May 2025 | **Revised:** 30 July 2025 | **Accepted:** 22 September 2025

Handling Editor: Igor Timoshkin

Funding: This work was financially supported by National Recovery and Resilience Plan (NRRP), Mission 04 Component 2 Investment 1.5—NextGenerationEU Award number: 0001052.

Keywords: electrospinning | nanofibres | nanostructured materials | scanning electron microscopy | tensile strength | thermal stability

ABSTRACT

This study investigates the physical-chemical and electrochemical performances of innovative separators for Li-ion batteries based on poly(vinylidene fluoride-hexafluoropropylene) (PVDF-HFP) nanofibrous membranes. The nanofibrous mat is produced through the electrospinning process, ensuring high surface to volume (S/V) ratio and allows large-scale production under suitable conditions. The materials investigated in this work aim at overcoming some limitations specific to the commercial separators, for example, mechanical shrinkage and electrolyte uptake. This is achieved by adding nanoparticles of different types, for example, ZrO_2, SnO_2, SiO_2 at different concentrations. Results claim that nanofibrous separators improve the mechanical and thermal stability of the mat without significantly impacting its electrochemical performances. In particular, the addition of 7 wt% of ZrO_2 nanoparticles to the nanofibrous separator showed to outperform commercially available solutions (i.e., Celgard) in terms of mechanical and thermal stability exhibiting, also, electrochemical performances.

1 | Introduction

Nowadays, the need for high performance and high reliability Li-ion batteries is a fundamental activity for the proper penetration of Renewable Energy Sources (RES) into the energy mix. Over the past decades, new technologies and materials have been investigated and used for this purpose leading to new cells capable of providing high power and energy when required [1–3].

Although extensive exploration of different electrode materials has been widely investigated in literature [4–7], giving access to higher voltages and the overcoming of some material limitations such as dendrites in the case of Li-met cells, the focus on alternative materials for electrolytes and separators remains limited.

In the overall cell structure, separators play a crucial role in ensuring physical separation between anode and cathode, allowing ionic transport while preventing electronic conduction. In particular, the achievement of optimal electrolyte absorption is essential to guarantee the high performance of these batteries.

Separators must ensure high thermal and mechanical stability, as well as safety, under a wide range of operating conditions.

This is an open access article under the terms of the Creative Commons Attribution License, which permits use, distribution and reproduction in any medium, provided the original work is properly cited.

© 2025 The Author(s). *IET Nanodielectrics* published by John Wiley & Sons Ltd on behalf of The Institution of Engineering and Technology.

With reference to electrical properties, separators must ensure high ionic conductivity as well as low electronic conductivity. This allows the desired REDOX reactions to occur with the maximum efficiency [8].

In the literature on batteries, ionic conductivity is often evaluated through the use of the MacMullin number (N_M) [9, 10], which relates the resistivity of the electrolyte and separator assembly to the one of the electrolyte. Generally, the best expected performance for batteries occurs when N_M is as low as possible (in any case higher than the electrolyte only $N_M = 1$).

Under rated conditions, Li-ion batteries may be subjected to a wide temperature range and all their components should be able to withstand such conditions. Moreover, if a fault occurs, high currents can flow in the cell, leading to localised high temperatures that could compromise the integrity of the separator. In these circumstances, electrode short circuits occur, causing serious damage to the battery and, in some cases, a potential fire hazard [11, 12]. Moreover, the trend of increasing energy density of current batteries implies the need of high-temperature resistant and high-performance materials.

In this context, novel materials designed for use as separators have been developed to address the abovementioned issues and enhance performance and thermal stability. Most of these innovative materials are derived from polyolefin-based compounds such as polyethylene (PE), polypropylene (PP) and their blends, ensuring excellent electrical and mechanical properties [13–15]. For instance, Celgard is a commercially-available separator characterised by a three-layer structure (PP/PE/PP) which ensures passive safety when an abrupt increase of temperature occurs due to for example, high currents (thermal runaway) [16]. Celgard stands out as an excellent separator thanks to its remarkable electrical and mechanical properties, making it a widely adopted choice in Li-ion batteries. On the other hand, polyolefin-based materials are characterised by a high N_M, low porosity and low electrolyte uptake, significantly limiting the application of this type of separators.

For this reason, the manufacturing of material implying different matrixes for example, polyvinylidene fluoride (PVDF) and structures (e.g., fibre-reinforced matrixes) along with the incorporation of inorganic fillers, is widely studied in literature as a possible approach at overcoming these limitations [17–23]. In particular, PVDF and its copolymer are characterised by the presence of highly polar C–F molecules and a semi-crystalline structure. These electronegative molecules ensure strong electron-withdrawing which is highly desirable in the case of batteries. With reference to the structural arrangement, the crystalline phase has been proved in literature to guarantee adequate mechanical integrity, while the amorphous one contributes to the capture of liquid electrolytes and to successful ionic conduction [24, 25].

These PVDF-specific properties may be enhanced when the material is in form of nanofibrous mat combined with inorganic nanofillers [18, 26–29]. Nanofibrous mats of PVDF-based materials may be obtained through the electrospinning technique. Membranes prepared via electrospinning exhibit high porosity and surface to volume ratio, controllable thickness along with a unique complex structure, leading to an overall enhancement of the separator properties.

In terms of porosity, nanofibrous mats typically exhibit values in the range of approximately 70%–80%. It enables excellent electrolyte uptake by providing a large surface area and interconnected pore network, which facilitates rapid ion transport throughout the membrane. At the same time, the porous structure effectively hinders electron conduction, acting as an insulating barrier that prevents short circuits and enhances the overall safety and efficiency of the system [30, 31].

Even so, nanofibrous mats are characterised by very low mechanical and thermal stability. For this reason, the addition of different nanofillers has been already investigated in literature aiming at improving the electrical and mechanical properties, including ionic conductivity, mechanical strength and thermal stability [32]. Among them, various ceramic oxides have been extensively studied due to their ability to withstand high temperatures. For instance, the addition of silicon dioxide (SiO_2) into PVDF-based nanofibres has been observed to improve not only the thermal stability but also the electrochemical properties of the separator [18, 33–35], while zirconium oxide (ZrO_2) has been found to enhance the electrolyte wettability [36–38]. Moreover, the addition of Al_2O_3 improve the electrochemical performance of lithium-ion battery (LIB) separators [35, 39].

However, despite some noteworthy advancements, there is still a remarkably gap in the existing literature in providing a comprehensive analysis of the most promising ceramic nanoparticles, encompassing the mechanical, thermal and electrochemical performance of the separator. Under these circumstances, this study aims at providing a complete analysis of the characteristics of PVDF-based nanofibrous separators that is, PVDF-HFP (hexafluoropropylene) with the incorporation of three different ceramic additives: zirconium oxide (ZrO_2), silicon oxide (SiO_2) and tin oxide (SnO_2), with different weight concentrations. This is accomplished through a multiscale analysis approach that spans from microscale physical-chemical tests to macroscale mechanical and electrochemical evaluations. The goal is to identify the optimal type and concentration of inorganic nanofillers for the nanofibrous mat separators, ensuring superior electro-thermal properties for high-performance lithium-ion battery applications.

2 | Experimental Section

The following sections describe the preparation of separators and their mechanical and electrochemical characterisation. Nanofibrous mats were fabricated through electrospinning starting from a polymeric solution in which ceramic nanoadditives were dispersed. Subsequently, the separators were characterised using microscopy techniques to assess the uniformity of additive dispersion. Following this, thermal and mechanical tests, including tensile test, thermal shrinkage analysis and electrolyte uptake measurements, were conducted to determine the performance of the separators. Finally, the separators were assembled in coin batteries and subjected to cycling and ionic conductivity tests.

25143255, 2025, 1, Downloaded from https://ietresearch.onlinelibrary.wiley.com/doi/10.1049/ndc2.70021 by Area Sistemi Dipart & Doc, Wiley Online Library on [31/10/2025]. See the Terms and Conditions (https://onlinelibrary.wiley.com/terms-and-conditions) on Wiley Online Library for rules of use; OA articles are governed by the applicable Creative Commons License

2.1 | Preparation of the Nanofibrous Separators

Three different solutions were prepared by dispersing the ceramic nanofillers (*Zirconium Oxide Nanopowders*, ZrO_2, 30 nm, high purity 99.95+%, *Tin Dioxide Nanoparticles*, SnO_2, 30–60 nm, high purity 99.87%, *Silicon Dioxide Nanoparticles*, SiO_2, 15–35 nm, amorphous, purity 99.5+%, provided by Nanografi Nano Technology) in N, N′-dimethyl acetamide (DMAc). Through an ultrasonicator (Hielscher UP200St) operating at 50 W for 30 min a homogeneous dispersion was achieved and an ice bath was used to minimise the solvent evaporation. Subsequently, PVDF-HFP (Kynar flex 2801, Arkema, $M_w = 4.77 \times 10^5$) at a concentration of 16 wt% was added to the sonicated solutions. Acetone (AC) and DMAc were used as solvents in a weight ratio of 70:30 and for each nanofillers, three different solutions were prepared by changing the additive concentration. To ensure complete mixing, the solutions obtained were stirred for 5 h. Table 1 reports the solutions prepared with different weight concentrations of nanoadditive. For ZrO_2 and SnO_2, the chosen additive concentrations were 5, 7, and 10 wt%. However, due to the high volume-to-weight ratio of SiO_2, preparing a solution with the same additive concentration was not feasible. Higher concentrations could lead to the formation of beads, which are attributed to the agglomeration of silica within the electrospun nanofibres [40]. To overcome this, the concentration of silica was reduced by a factor of ten.

The electrospinning setup (Spinbow Lab Unit, Spinbow S.r.l., Italy) used in this study consist of four high-voltage needles and a low-speed rotating drum connected to the ground. The polymeric solution was pumped into a syringe and the process took place at a flow rate of 1.3 mL/h. A high voltage of 20 kV was applied to the needles, creating an instability region between the high voltage needles and the ground collector, which facilitated the stretching of the polymer solution. The manufactured nanofibres were randomly collected on the drum, rotating at 50 rpm and placed at 17 cm from the needles, under conditions of 25°C and 50% relative humidity.

After electrospinning, the nanofibrous mats were placed in an oven at 90°C to remove any residual solvents and compressed under 2 kg weight to improve handling. This post-treatment resulted in a final nanofibre thickness of approximately 40 μm.

TABLE 1 | Prepared solution with different weight percentage of ZrO_2, SnO_2, and SiO_2 nanoparticles.

Nanoadditive	Concentration in the final solution (wt%)
Neat	—
ZrO_2	5
	7
	10
SnO_2	5
	7
	10
SiO_2	0.5
	0.7
	1

2.2 | Separator Characterisation

The morphology of the nanofibrous mats were evaluated through a Field Emission Scanning Electron Microscope (FE-SEM, Tescan Mira3) and a Transmission Electron Microscope (TEM, Philips CM 100). The element distribution and the chemical composition of the different separators were investigated through Energy-Dispersive X-ray spectroscopy (EDX) and Fourier-Transform Infrared spectroscopy (FTIR, PerkinElmer Spectrum II), respectively. The FTIR spectra were recorded in ATR (attenuated total reflectance) mode and after the acquisition, raw data were normalised with respect to the amplitude of the peak corresponding to the stretching vibrational mode of the C–F at 1400 cm^{-1}.

The mechanical properties were examined by a universal tensile testing machine (Remet TC-10) equipped with a 10 N load cell, speed test 10 mm/min. To ensure secure handling and prevent slippage of the nanofibrous mats, the tensile samples were prepared by affixing the mat to a paper frame. This guaranteed that all the nonwoven fibres were clamped in the machine. The final sample dimensions were 20 × 45 mm, (width × initial length) and the paper frame was cut before test started as described in ref. [41]. At the end of the test the specimen was retrieved and weighted to calculate the stress σ_m according to:

$$\sigma_m = \frac{\rho_m \cdot F \cdot L_0}{m} \text{ [MPa]}, \quad (1)$$

where ρ_m is the material density (mg/mm3), m denotes the mass of the tested sample (mg), L_0 indicates the initial length of the specimen (mm), and F represents the applied force (N). Stress-strain curves were generated from a minimum of five samples for each type of nanofibrous mat. The strain ε was determined as follows:

$$\varepsilon = \frac{(L - L_0)}{L_0} \text{ [–]}, \quad (2)$$

where $(L - L_0)$ represents the observed change in length during the test. The elastic modulus (E) was calculated by determining the slope of the tangent to the initial linear region of the stress-strain curve.

The thermal stability of the separator was assessed by measuring the shrinkage A of a 20-mm diameter circular specimen using the following equation:

$$A = \frac{(D_0 - D)}{D_0} \cdot 100 \text{ [\%]}, \quad (3)$$

where D_0 and D represent the diameter of the sample before and after the test, respectively. Experiments were conducted over a temperature range of 50°C–150°C in 20°C intervals, with each test lasting 30 min.

25143255, 2025, 1, Downloaded from https://ietresearch.onlinelibrary.wiley.com/doi/10.1049/ndc2.70021 by Area Sistemi Dipart & Doc, Wiley Online Library on [31/10/2025]. See the Terms and Conditions (https://onlinelibrary.wiley.com/terms-and-conditions) on Wiley Online Library for rules of use; OA articles are governed by the applicable Creative Commons License

The electrolyte uptake of the separator was evaluated by soaking the specimen into the electrolyte solution, LP71, 1 M of Lithium hexafluorophosphate $LiPF_6$ in 1:1:1 wt:wt:wt Ethylene Carbonate (EC):Dimethyl Carbonate (DMC):Diethyl Carbonate (DEC), used to assemble the LIB. The separator weight was measured before (M_{dry}) and after (M_{wet}) the immersion and the electrolyte uptake was calculated according to:

$$U = \frac{(M_{wet} - M_{dry})}{M_{dry}} \cdot 100\ [\%]. \quad (4)$$

2.3 | Electrochemical Analysis

The resistivity of the electrolyte-saturated separators was determined through Electrochemical Impedance Spectroscopy (EIS). To perform this test, a Solartron SI 1255 frequency response analyser coupled with an EG&G Model 273A PAR potentiostat/galvanostat and Biologic VSP were employed. In the EIS procedure, the separator, pre-soaked in the electrolyte (LP30 with a resistivity of 82.5 Ω·cm [42]) was placed between two stainless steel (SS) blocking electrodes with an area of 0.785 cm^2 and arranged within a T-shaped Teflon cell (BOLA by Bohlender GmbH). The MacMullin number N_M was calculated by applying an AC voltage of 5 mV at the frequency range from 10^5 to 0.1 Hz at 30°C, using the equation:

$$N_M = \frac{\rho_{s+e}}{\rho_e}\ [-], \quad (5)$$

where ρ_{s+e} denotes the resistivity of the electrolyte/separator assembly under consideration and ρ_e the resistivity of the electrolyte solution.

The performance of batteries with different separators was evaluated by assembling cells consisting of a graphite anode on a copper substrate, a $LiFePO_4$ cathode on aluminium foil (supplied by MTI Corporation), and an electrolyte composed of 1 M $LiPF_6$ in ethyl carbonate, dimethyl carbonate and diethyl carbonate (purchased from TmaxCN) in a 1:1:1 volume ratio ($LiFePO_4$/separator/graphite, 1.0 M $LiPF_6$ in EC:DEC:DMC = 1:1:1, v/v/v). Because of the high reactivity of the lithium, the cells were assembled in an argon-filled glove box and tested at 25°C over a voltage range of 2.7–3.6 V. To evaluate the rate capability, the cells were cycled at varying current densities from 0.1C to 1C (0.1C, 0.2C, 0.5C and 1C), with the initial charge/discharge cycle performed at a low current of 0.05C to stabilise the battery.

3 | Results and Discussion

3.1 | Micrograph Analysis

The different nanofibrous mats were examined through SEM and the resulting micrograph analysis are shown in Figure 1a–i. As observed from the pictures, generally high concentrations of nanoadditives in the polymeric solution increase the number and size of agglomerates within the fibres. This effect is particularly evident in the ZrO_2-filled nanofibres (Figure 1a–c), where higher concentration of nanoparticles creates a coating that covers the PVDF-HFP nanofibres, thereby increasing their thickness. By using an image analysis software (ImageJ), 100 nanofibers per magnification were analysed and the resulting average diameters are displayed in Table 2. As shown in the table, increasing the amount of nanoadditives leads to a thicker nanofibre diameters. However, while the rise is moderate for the SnO_2 and SiO_2 nanofibrous mats, in the case of nanofibres with the addition of ZrO_2, a concentration of 10 wt% of nanoadditive results in an approximately 93% increment in the average fibre diameter compared to the previous case (7 wt% of ZrO_2).

Moreover, TEM was employed to investigate the morphology and nanoparticle distribution within electrospun nanofibrous separators. The fibres were deposited onto conventional copper micro-grids and analysed using a Philips CM 100 TEM operating at 60 kV. This technique enables the identification of inorganic nanoparticles embedded within or adhered to the surface of the organic polymer matrix, where the inorganic phase appears as dark contrast regions (black spots) against the lighter polymer background. As shown in Figure 2a, the pristine sample exhibits a uniform fibrous structure with no visible inclusions, serving as a reference. In contrast, the samples containing 10 wt% ZrO_2, 10 wt% SnO_2 and 1 wt% SiO_2 display a clear presence of nanoparticles distributed along the fibre length. Figure 2b highlights the presence of ZrO_2 particles in a coating-like structure on the PVDF-HFP nanofibres, leading to an increase in fibre diameter, as also confirmed by SEM imaging. Fibres containing 10 wt% SnO_2 and 1 wt% SiO_2 (Figure 2c,d, respectively) exhibit aggregated nanoparticles, some of which protrude from the fibre surface.

3.2 | Characterisation of the Separators

3.2.1 | Chemical Characterisation

To evaluate the correct nanofiller dispersion in the nanofibrous mats after the electrospinning process, the separators were characterised using EDX and FTIR spectroscopy. The first technique is an analytical method used for the elemental analysis of the sample. Results are reported in Figure 3. As expected, the main peaks recorded for the neat sample are C, F and Au (left graph of Figure 3). This latter is related to the gold metallisation required for the proper analysis of the sample within the EDX-SEM instrumentation. Spectra are modified in the case of nanofilled materials, showing new peaks related to the characteristic elements of the considered nanofillers that is, Si, O and Sn. No new peak can be recorded for Zr since its energy is centred on the same level as Au. To complement the EDX spectra, the right panel of Figure 3 displays the elemental dot maps that visualise the spatial distribution of the fillers within the polymer matrix. As observed, the concentration of zirconium—attributable to the presence of ZrO_2 nanoparticles—is markedly higher compared to the other samples. This finding is consistent with the results obtained from SEM and TEM analyses. The incorporation of ZrO_2 appears to form a coating-like layer on the nanofibres, resulting in a pronounced accumulation of zirconium at the fibre surface. In contrast, the SiO_2 nanoparticles exhibit the lowest dot

25143255, 2025, 1, Downloaded from https://ietresearch.onlinelibrary.wiley.com/doi/10.1049/ndc2.70021 by Area Sistemi Dipart & Doc, Wiley Online Library on [31/10/2025]. See the Terms and Conditions (https://onlinelibrary.wiley.com/terms-and-conditions) on Wiley Online Library for rules of use; OA articles are governed by the applicable Creative Commons License

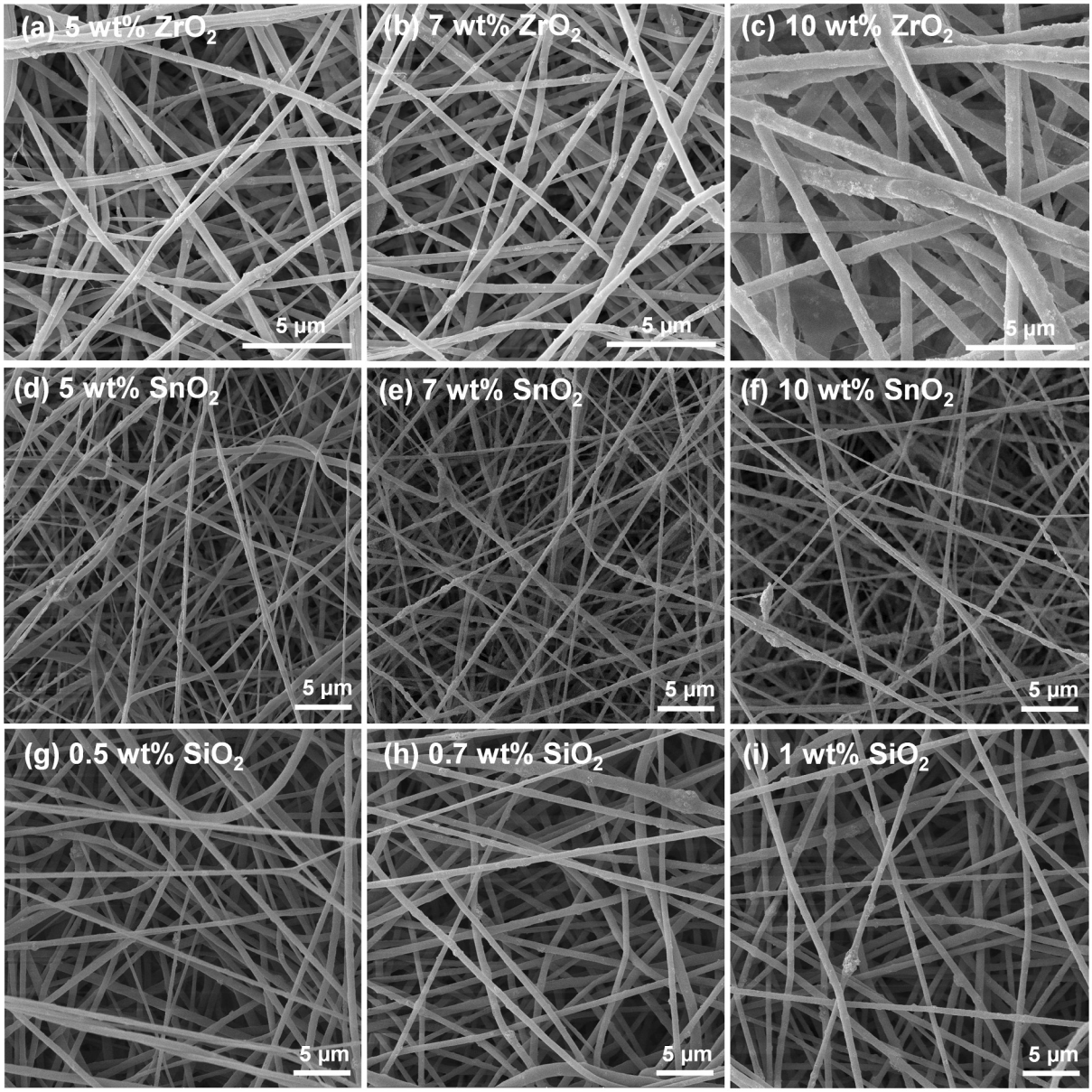

FIGURE 1 | SEM magnification of PVDF-HFP nanofibres with different nanoadditive concentration: 5 wt% (a), 7 wt% (b), and 10 wt% (c) of ZrO_2, 5 wt% (d), 7 wt% (e), and 10 wt% (f) of SnO_2, and 0.5 wt% (g), 0.7 wt% (h) and 1 wt% (i) of SiO_2.

TABLE 2 | Nanoadditive concentration and final average fibres diameter.

Nanoadditive	Concentration (wt%)	Average fibres diameter (nm)
Neat	—	302 ± 134
ZrO_2	5	332 ± 62
	7	375 ± 158
	10	724 ± 150
SnO_2	5	370 ± 102
	7	411 ± 104
	10	419 ± 72
SiO_2	0.5	585 ± 100
	0.7	601 ± 81
	1	661 ± 117

density in the elemental maps, likely due to a concentration 10 times lower than that of the other fillers. Furthermore, quantitative data derived from EDX-SEM analysis allow for the calculation of atomic ratios, which provide insight into the molar contributions of each element within the selected region of interest.

To investigate the chemical groups within the materials, nanofibrous mats were analysed through FTIR spectroscopy and the results are depicted in Figure 4. Measurements were conducted for each additive concentration and compared with the neat sample (pure PVDF-HFP mat) within the wavenumber range of 1500 to 450 cm^{-1}, where significant changes in the absorbance spectrum are observable.

All curves were normalised with respect to the amplitude of the peak corresponding to the stretching vibrational mode of the C–F at 1400 cm^{-1} [43]. This peak is associated with the crystalline

25143255, 2025, 1, Downloaded from https://ietresearch.onlinelibrary.wiley.com/doi/10.1049/ndd2.70021 by Area Sistemi Dipart & Doc, Wiley Online Library on [31/10/2025]. See the Terms and Conditions (https://onlinelibrary.wiley.com/terms-and-conditions) on Wiley Online Library for rules of use; OA articles are governed by the applicable Creative Commons License

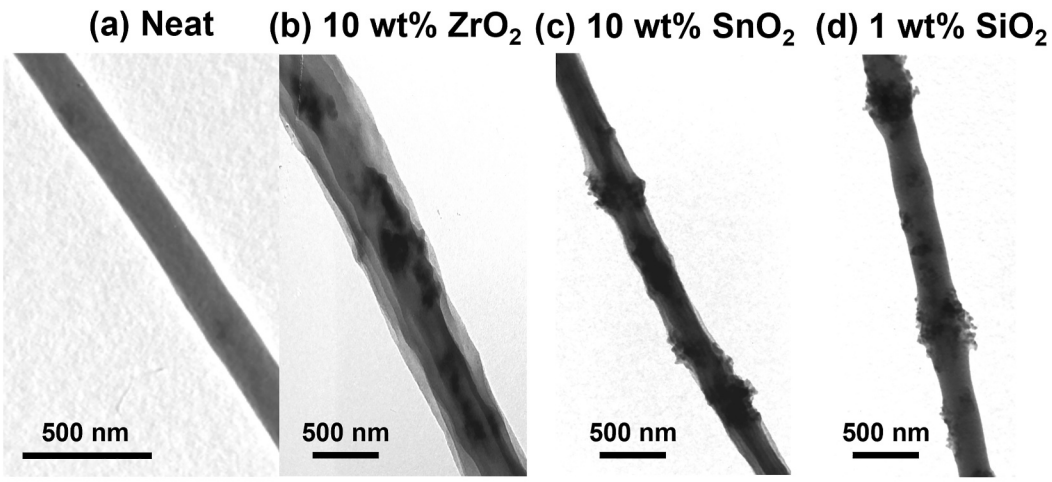

FIGURE 2 | TEM images of electrospun PVDF-HFP nanofibres with varying compositions: (a) neat PVDF-HFP, (b) PVDF-HFP with 10 wt% ZrO_2, (c) PVDF-HFP with 10 wt% SnO_2 and (d) PVDF-HFP with 1 wt% SiO_2.

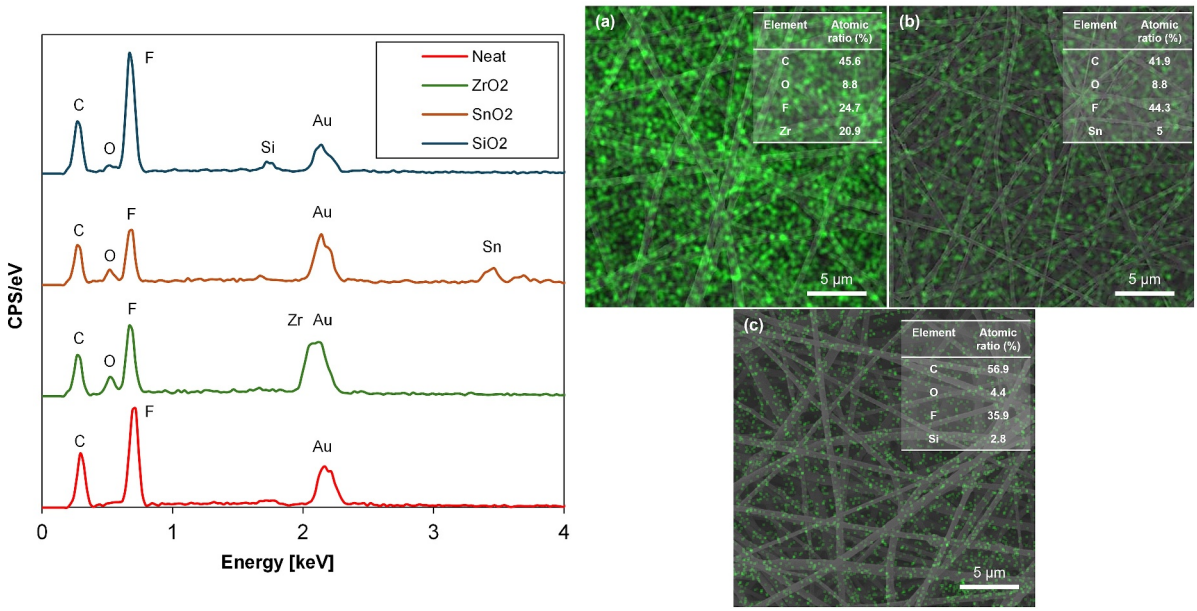

FIGURE 3 | EDX graph for each type of nanofilled separator (left) and elemental dot maps (right) for (a) 10 wt% ZrO_2, (b) 10 wt% SnO_2 and (c) 1 wt% SiO_2.

β-phase of the PVDF-HFP and remains unchanged after the nanofiller addition. Although it does not represent a quantitative analysis, this normalisation approach not only confirms the successful integration of nanoparticles but also facilitates a consistent comparison across samples with varying filler concentrations.

The possible band assignment for the most relevant peaks of PVDF-HFP and the nanofillers ZrO_2, SnO_2 and SiO_2 were reported in Table 3. For instance, peaks related to the electroactive β-phase include those at 1276, 1179, 1062, 841, 600, 487 cm^{-1}, whereas the vibrational bands at 879, 740 and 510 cm^{-1} are attributed to the nonpolar α-phase. Additionally, samples with varying concentrations of ZrO_2 nanoparticles (graph of Figure 4a) exhibit peaks at 743, 579 and 505 cm^{-1}, whose intensity follows the particle concentrations. Similar behaviour is recorded in Figure 4b where peaks associated with SnO_2 (609 and 468 cm^{-1}) are present and in Figure 4c for samples with SiO_2 nanoparticles (1082, 808, and 468 cm^{-1}). It is worth highlighting that the intensities of the new peaks associated with the SiO_2 nanoadditives are significantly lower compared to those observed for the other two fillers. This difference can be ascribed to the lower concentration of SiO_2.

3.2.2 | Mechanical Properties

During the assembly process and during their operation, batteries have to withstand mechanical and thermal stresses that can lead to separator failure and thus short-circuit the battery. For this reason, mechanical and thermal properties of nanoadditive separators were analysed, specifically mechanical deformation by tensile test, resistance to high temperatures by thermal shrinkage test, and shrinkage of the nanofibrous mat as a result of electrolytic adsorption by uptake test.

25143255, 2025, 1, Downloaded from https://ietresearch.onlinelibrary.wiley.com/doi/10.1049/ndc2.70021 by Area Sistemi Dipart & Doc, Wiley Online Library on [31/10/2025]. See the Terms and Conditions (https://onlinelibrary.wiley.com/terms-and-conditions) on Wiley Online Library for rules of use; OA articles are governed by the applicable Creative Commons License

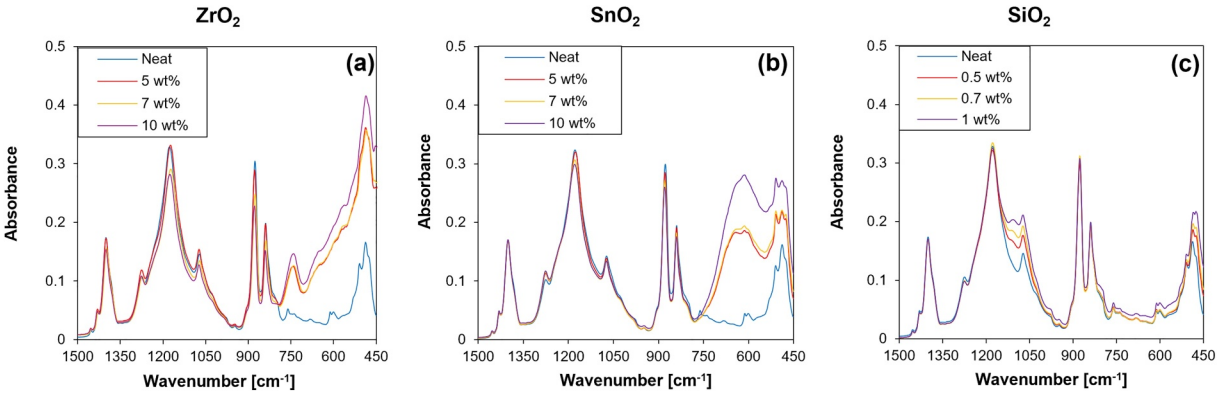

FIGURE 4 | FTIR spectra for nanofibrous mats with different content of nanofiller: (a) ZrO_2, (b) SnO_2 and (c) SiO_2.

TABLE 3 | Possible assignments of significant peaks in FTIR spectra of PVDF-HFP, ZrO_2, SnO_2 and SiO_2.

Material	Wavenumber (cm^{-1})	Possible assignment	References
PVDF-HFP	487	CF_2 wagging	[44]
	510, 740, 879	α-phase	[44]
	600	CF symmetrical stretching	[45]
	841	CH_2 rocking	[46]
	1062	CC skeletal vibration	[43]
	1179	CF_3 symmetrical stretching	[43]
	1276	CF_2 symmetrical stretching	[44]
	1400	CF stretching	[43]
ZrO_2	505, 579, 743	Stretching and bending vibrations	[47]
SnO_2	609	O–Sn–O stretching vibration	[48]
	468	Sn–O stretching vibration	[48]
SiO_2	468	Si–O–Si rocking vibrational	[49]
	808	O–Si–O bending	[49]
	1082	Si–O asymmetric stretching	[49]

The stress-strain curves obtained from tensile tests, performed on five samples for each mat type, are presented in Figure 5. These graphs display the tensile curves for the analysed fillers, compared to the curve generated by the pure PVDF-HFP mat. As shown in Figure 5a, the addition of ZrO_2 increases the maximum stress (σ_{max}) applicable to the material but slightly reduces the elongation at break compared to the neat sample. Similar results were obtained for the samples filled with SnO_2 (Figure 5b); however, the maximum strain (ε_{max}) is significantly lower than that of the pure specimen. For the silicon oxide-filled specimens shown in Figure 5c, adding small nanoparticle concentrations (0.5 and 0.7 wt%) improves the maximum elongation. On the contrary, higher weight percentage (1 wt%), causes the increase of stress at break, but it reduces the maximum elongation of the specimen.

What just described may be easier highlighted by considering some parameters extracted from the stress-strain curves and presented in Figure 6 and in Table 4 that is, stress at break σ_{max} (Figure 6a), elongation at break ε_{max} (Figure 6b) and Young's modulus (Figure 6c).

From Figure 6 it is evident how the introduction of fillers modifies all the mechanical properties of the neat sample. In general, the addition of nanoparticles slightly improves the stress at break. In the case of ZrO_2, the lowest concentration causes the biggest increase of the property (~ +25%), while higher concentrations reduce the value to 28 MPa (close to the neat value). This may be likely imputed to the agglomeration of fillers for concentrations ≥ 7 wt%. The tin oxide filler brings to the increase of σ_{max} to around 32 MPa, with the value kept constant with concentration. With weight percentages of SiO_2 lower than 1, results claim no variation of the property, while higher quantity causes its rise (+20%).

With reference to the elongation at break, very little modifications are recorded with additive concentration for ZrO_2 and SnO_2 filled samples, showing the lowest value for the tin oxide-filled specimens (above 50% reduction). In the case of silica, a significant increase of the property is recorded for concentrations up to 0.7 wt%, while the highest amount here considered (1 wt%) brings back the value to the neat one.

25143255, 2025, 1, Downloaded from https://ietresearch.onlinelibrary.wiley.com/doi/10.1049/ndc2.70021 by Area Sistemi Dipart & Doc, Wiley Online Library on [31/10/2025]. See the Terms and Conditions (https://onlinelibrary.wiley.com/terms-and-conditions) on Wiley Online Library for rules of use; OA articles are governed by the applicable Creative Commons License

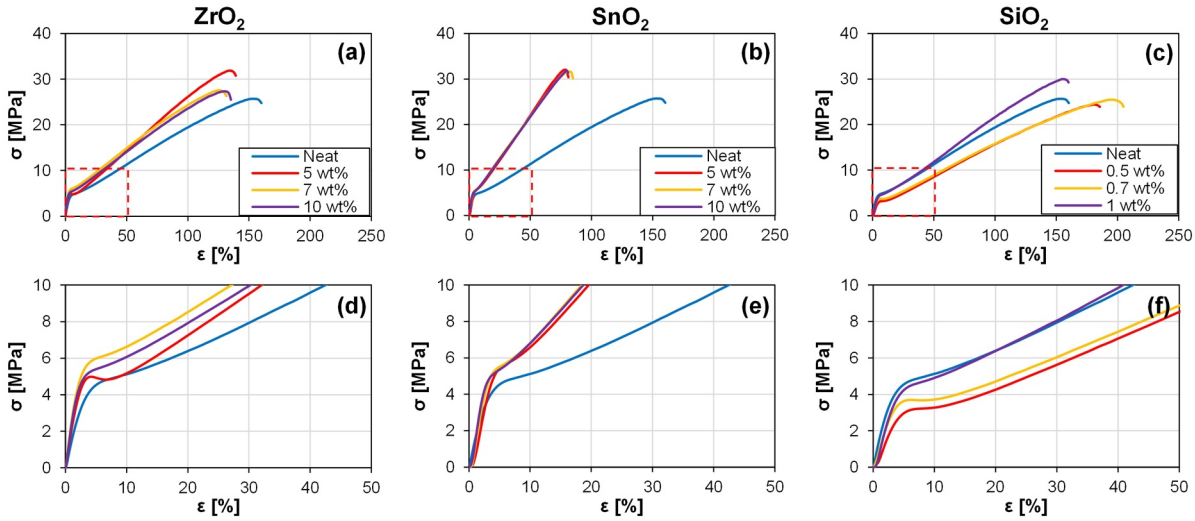

FIGURE 5 | Stress-strain curves for different quantities of: ZrO_2 (a—full graph, d—insight), SnO_2 (b—full graph, e—insight) and SiO_2 (c—full graph, f—insight).

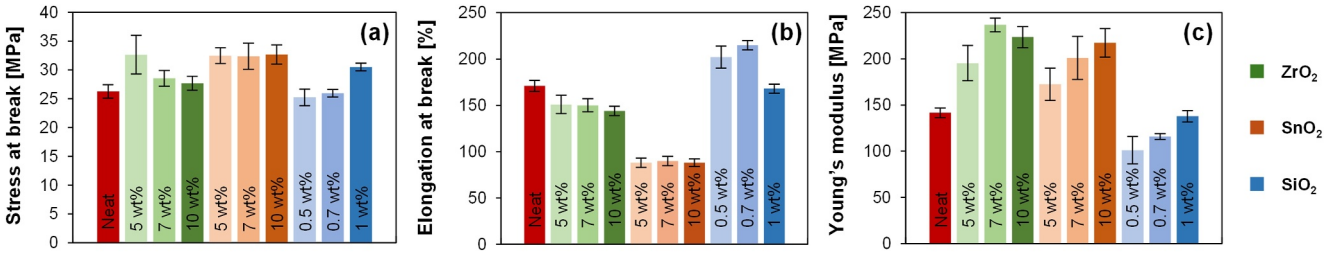

FIGURE 6 | Mechanical parameters as a function of different filler percentages. (a) Stress at break, (b) elongation at break and (c) Young's modulus.

The elastic modulus E shows a monotonic increase with the amount of nanoparticles. Only in the case of SiO_2, a reduction of the property is observed at 1 wt%, where the value returns to its original pristine level.

To sum up, depending on the type of nanofillers, different behaviours may be drawn. In general, if no agglomeration occurs, the nanostructured materials result to be stiffer with improved maximum stress at break (tensile strength) and reduced maximum elongation. Agglomeration of nanoparticles may be seen for concentrations > 7 wt% in the case of ZrO_2 and 1 wt% for SiO_2. Introduction of SnO_2 nanofillers causes the halving of the maximum elongation at break but no modifications with concentration is seen for the percentages here considered, suggesting that either agglomeration did not occur, or it is already present for the lowest filler amount (5 wt%).

Eventually, the Young Modulus shows a significant increase with the introduction of ZrO_2 and SnO_2 nanofillers. The increase is found to be monotonic for all the materials here considered, except for the 10 wt%-filled ZrO_2 material, where a slight decrease of the Modulus (~5%) is recorded in comparison to the lower concentration (7 wt%). The addition of 0.5 wt% SiO_2 causes the decrease of the Young modulus (~ −50%), while 1 wt% brings to the same value measured on the neat material.

Table 5 reports the percentual variation in size for the specimens under test after the thermal shrinkage treatment. Figure 7 provides pictures illustrating the dimensional shrinkage for materials that showed the best shrinkage performance with each nanofiller content at various temperature steps. The neat nanofibrous mat (Figure 7a) shows great thermal stability up to 130°C, unlike commercial separators such as Celgard, which exhibit over 90% shrinkage at this temperature due to the melting of the polyethylene layer. However, at 150°C, the neat mat undergoes significant shrinkage (~80%). The addition of zirconium dioxide allows very low shrinkage percentage values to be obtained, with a reduction of less than 25% of the initial dimension, as evident in Figure 7b. For the SnO_2, low filler concentrations (5 and 7 wt%) result in similar shrinkage value of the pure PVDF-HFP specimen (A = 80%), while the highest amount (10 wt%, Figure 7c) lead to a shrinkage percentage of 71%. Finally, the silica additive seems to have no impact on sample shrinkage, with results comparable to those of the neat sample as shown in Figure 7d.

3.2.3 | Electrolyte Uptake

Table 6 presents the electrolyte uptake (U [%]) for various concentrations of ZrO_2, SnO_2, and SiO_2 nanofillers, as well as the neat PVDF-HFP mat. For ZrO_2-filled nanofibres, a clear decrease in electrolyte uptake is evident as the filler concentration increases, with a reduction from 505% ± 8% in the neat sample to 345% ± 57% at 10 wt% ZrO_2. This indicates that higher

25143255, 2025, 1, Downloaded from https://ietresearch.onlinelibrary.wiley.com/doi/10.1049/ndc2.70021 by Area Sistemi Dipart & Doc, Wiley Online Library on [31/10/2025]. See the Terms and Conditions (https://onlinelibrary.wiley.com/terms-and-conditions) on Wiley Online Library for rules of use; OA articles are governed by the applicable Creative Commons License

TABLE 4 | Stress-strain data for different additive concentration.

	Neat	5 wt% ZrO_2	7 wt% ZrO_2	10 wt% ZrO_2	5 wt% SnO_2	7 wt% SnO_2	10 wt% SnO_2	0.5 wt% SiO_2	0.7 wt% SiO_2	1 wt% SiO_2
σ_{MAX} [MPa]	26 ± 1	33 ± 3	28 ± 1	28 ± 1	32 ± 1	32 ± 2	33 ± 2	25 ± 1	26 ± 1	30 ± 1
ε_{MAX} [%]	171 ± 6	151 ± 10	150 ± 7	144 ± 5	88 ± 5	90 ± 5	88 ± 4	202 ± 12	215 ± 5	168 ± 5
E [MPa]	141 ± 5	195 ± 19	237 ± 7	223 ± 11	172 ± 17	201 ± 23	217 ± 16	101 ± 14	116 ± 3	138 ± 6

TABLE 5 | Shrinkage percentages at $T = 150°C$ for all additive concentrations.

	Neat	5 wt% ZrO_2	7 wt% ZrO_2	10 wt% ZrO_2	5 wt% SnO_2	7 wt% SnO_2	10 wt% SnO_2	0.5 wt% SiO_2	0.7 wt% SiO_2	1 wt% SiO_2
A [%]	80 ± 2	35 ± 2	24 ± 3	36 ± 1	79 ± 2	77 ± 1	71 ± 2	82 ± 3	80 ± 2	80 ± 1

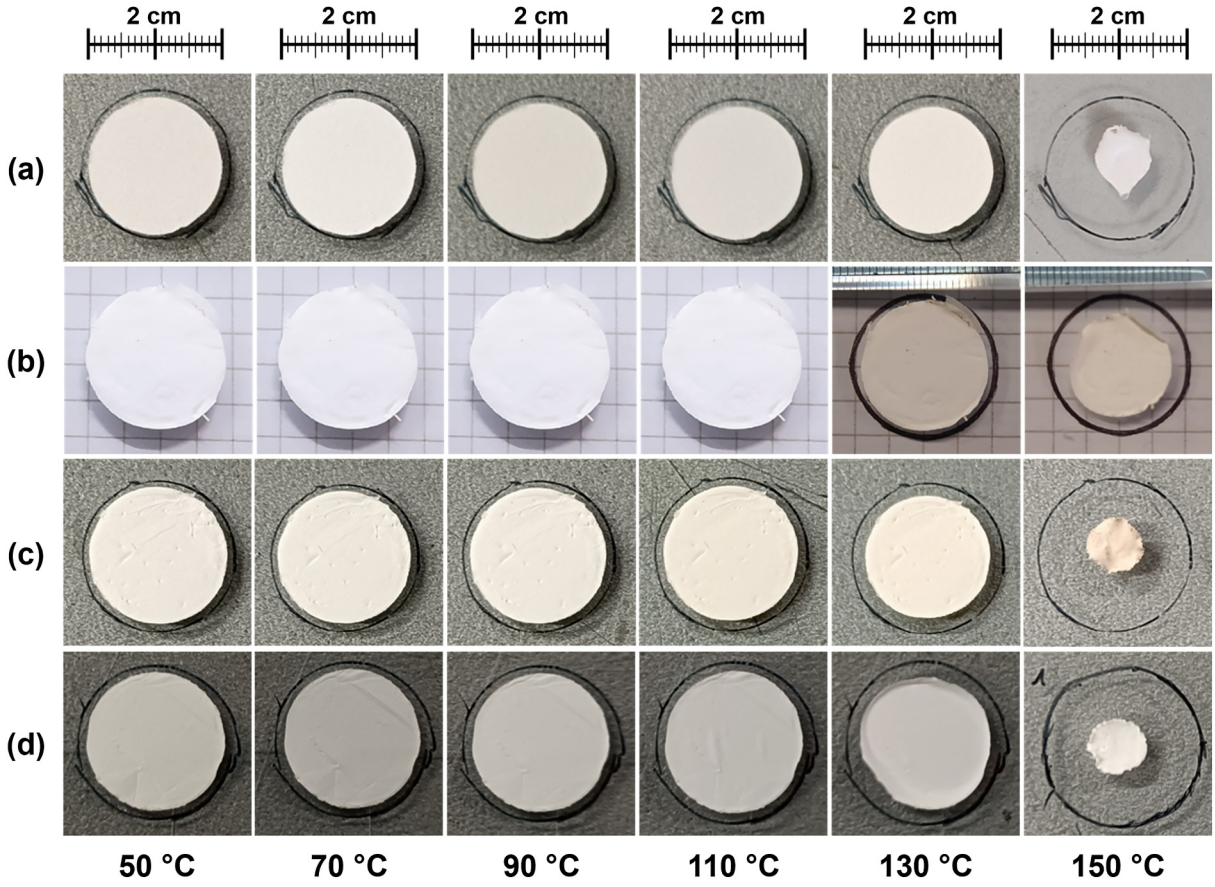

FIGURE 7 | Dimensional shrinkage of (a) pure PVDF-HFP, (b) 7 wt% of ZrO_2, (c) 10 wt% of SnO_2 and (d) 1 wt% of SiO_2.

TABLE 6 | Electrolyte uptake percentage for all additive concentration.

	Celgard	Neat	5 wt% ZrO_2	7 wt% ZrO_2	10 wt% ZrO_2	5 wt% SnO_2	7 wt% SnO_2	10 wt% SnO_2	0.5 wt% SiO_2	0.7 wt% SiO_2	1 wt% SiO_2
U [%]	78 [50]	505 ± 8	458 ± 62	381 ± 36	345 ± 57	327 ± 24	261 ± 34	247 ± 29	521 ± 91	400 ± 87	411 ± 52

concentrations of ZrO_2 reduce the material ability to absorb electrolytes, possibly due to the increased fibre diameter (Table 2) and the formation of a coating that limits electrolyte absorption (as shown also in the SEM magnification of Figure 1). Similar behaviour is seen for tin oxide-filled samples. Here, the electrolyte uptake decreases as the additive

25143255, 2025, 1, Downloaded from https://ietresearch.onlinelibrary.wiley.com/doi/10.1049/ndt2.70021 by Area Sistemi Dipart & Doc, Wiley Online Library on [31/10/2025]. See the Terms and Conditions (https://onlinelibrary.wiley.com/terms-and-conditions) on Wiley Online Library for rules of use; OA articles are governed by the applicable Creative Commons License

concentration increases, with values dropping to 247% ± 29% at 10 wt%. The more pronounced reduction compared to ZrO_2 suggests that SnO_2 have a greater impact on the electrolyte absorption, likely due to the different interactions between SnO_2 particles and the polymer matrix. In contrast, the silica nanofilled separators exhibit a different pattern. At the lowest concentration (0.5 wt%), the electrolyte uptake is slightly higher than that of the neat sample. However, as the concentration increases to 0.7 wt%, there is a significant drop to 400% ± 87%, followed by a slight increase to 411% ± 52% at 1 wt%. This nonlinear behaviour suggests that SiO_2 may initially enhance electrolyte uptake, but higher concentrations lead to a reduction, potentially due to changes in the fibre structure or porosity. All PVDF-HFP-based membranes show markedly higher electrolyte uptake compared to Celgard, which reaches only 78% [50]. Even the lowest-performing nanocomposite membrane more than doubles Celgard's value, while several formulations, including the neat and SiO_2-based samples, exceed 500%, highlighting a substantial advantage in absorption capacity.

3.3 | Electrochemical Performance

3.3.1 | Resistivity Analyses

The Nyquist plot of Figure 8 illustrates the results of the EIS tests in the low frequency region conducted on the Bola cell described in the Experimental section. As expected, all the obtained plots exhibit a linear behaviour. The electrolyte/separator resistance is determined from the EIS tests, with the bulk resistance of the separators corresponding to the intercept on the *x*-axis. Given the geometry of the separator, the corresponding resistivity ρ_{s+e} can be calculated using Ohm's law. Finally, the MacMullin number N_M is derived using Equation (5). Results are reported in Table 7.

In general, a low N_M number indicates reduced internal resistance, leading to enhanced battery performance. From Table 7 it is evident how the use of nanofibrous mats may strongly improve the parameter for the considering application. All PVDF-HFP-based membranes exhibit significantly lower MacMullin numbers compared to Celgard, which records a value of 17 [42]. The best-performing nanocomposite is reported to be the neat sample which reaches as low as 2.51, almost 7 times more favourable. Because the MacMullin number inversely correlates with ionic conductivity, these lower values directly indicate superior ion conduction through the composite membranes, reinforcing their potential for enhanced electrochemical performance. The zirconium oxide (ZrO_2)-filled separators show minimal variation in N_M with concentration, maintaining relatively low values (up to 4.14), suggesting that the filler does not significantly increase internal resistance, even at higher concentrations. In contrast, the addition of tin oxide and silica results in a clear trend of increasing N_M values with filler concentration. This trend is particularly pronounced at the highest concentrations—10 wt% for SnO_2 and 1 wt% for SiO_2—where N_M values reach 11.7 and 13.21, respectively. Nonetheless, these values are still lower if compared to that of commercial Celgard separator. The increase in N_M for these additives is likely due to the agglomeration of nanoparticles, which can hinder ion transport and increase internal resistance.

3.3.2 | Battery Cycling

The coin cell batteries assembled (described in the Experimental section) were cycled at different C-rate, along with a cell with commercial Celgard 2340 as separator. This cell was used as a reference to compare the behaviour with cells using nanofibrous separators. For the sake of clarity only the battery cycling results for the optimal concentration of each nanofiller are presented, based on the various concentrations tested: 7 wt% ZrO_2, 10 wt% SnO_2 and 1 wt% SiO_2.

In general, Figure 9 displays a significant improvement in the specific capacity for all the cells with nanofibrous separators in comparison to the Celgard one, for all the C-rates investigated.

Cells with nanofibrous separators exhibited similar discharge capacities of above 110 mAh/g at the lowest C-rate (C/10), except for the tin oxide-filled separator, which shows an increasing trend in specific capacity starting from a lower value

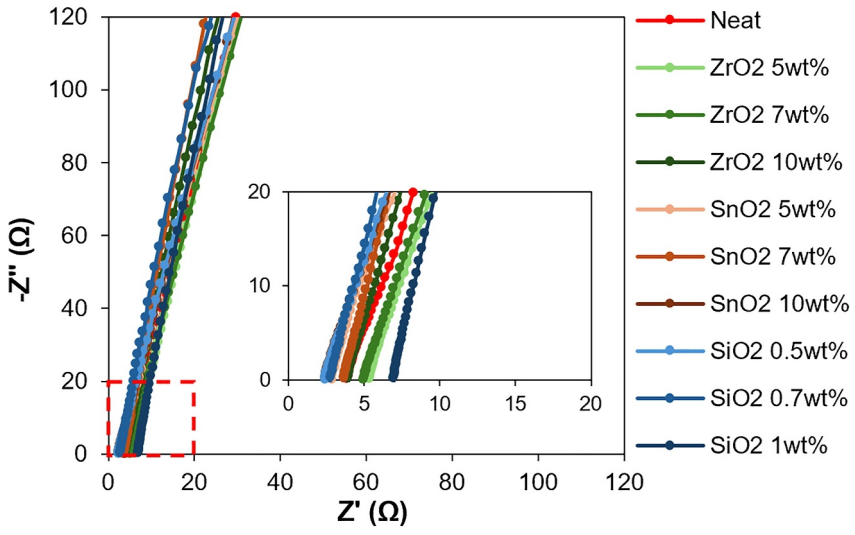

FIGURE 8 | Nyquist plot of the additive separators resulted from the EIS test in the low frequency region.

25143255, 2025, 1, Downloaded from https://ietresearch.onlinelibrary.wiley.com/doi/10.1049/nde2.70021 by Area Sistemi Dipart & Doc, Wiley Online Library on [31/10/2025]. See the Terms and Conditions (https://onlinelibrary.wiley.com/terms-and-conditions) on Wiley Online Library for rules of use; OA articles are governed by the applicable Creative Commons License

TABLE 7 | MacMullin number for different nanofilled separators.

	Celgard	Neat	5 wt% ZrO_2	7 wt% ZrO_2	10 wt% ZrO_2	5 wt% SnO_2	7 wt% SnO_2	10 wt% SnO_2	0.5 wt% SiO_2	0.7 wt% SiO_2	1 wt% SiO_2
N_M	17 [42]	2.51	3.93	4.14	3.12	5.00	5.74	11.7	4.31	5.09	13.21

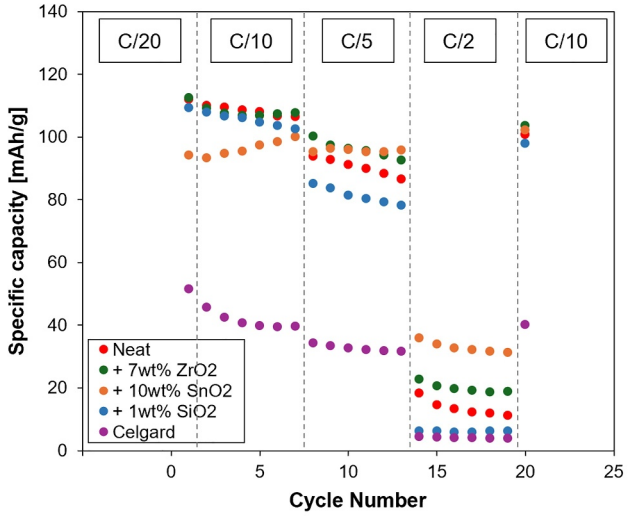

FIGURE 9 | Cycling performance at various C-rate for cells with different additive separators compared with Celgard.

of 95 mAh/g. This was likely imputed to the noncomplete stabilisation of the battery after the initial cycle at C/20. Higher rates (C/5) cause the drop in cell specific capacity, probably due to the limitations in migration of lithium ions. This capacity fade is more pronounced in the cell with SiO_2-filled separator, which shows a decrease of more than 30 mAh/g compared to the discharge at 0.1C. Furthermore, at a C-rate of 0.5C, the specific capacity of all cells drops sharply to very low values. Nonetheless, acceptable performances are recorded for C/2-rate. Here, the best performance is observed in the SnO_2-filled separator, exhibiting a capacity of above 40 mAh/g, whereas the silica-filled cells have the lowest performance, displaying a discharge capacity of merely 6 mAh/g. It is worth highlighting that, when compared to the battery with Celgard 2340 separator, the specific capacities of the nanofibrous separator cells are significantly higher, especially at lower currents. For instance, at C/10-rate, the specific capacity increases from 40 mAh/g in the Celgard cell to 110 mAh/g in the cells with nanofibrous separators. Tests at 1C are not reported, as the capacity dropped to zero in all cases. This result can not be attributed to the separator, since the commercial separator (Celgard) exhibited the same behaviour, but is more likely related to inefficiencies in the cathode. Furthermore, the last cycle performed at C/10, shows a capacity similar to that of the initial cycle, indicating that the batteries did not deplete during the cycling tests.

4 | Conclusion

The study investigates the development and characterisation of nanofibrous separators for LIBs by incorporating the ceramic nanofillers ZrO_2, SiO_2 and SnO_2 into a PVDF-HFP matrix. These separators aim to enhance thermal, mechanical and electrochemical properties, critical for high-performance and reliable batteries, along with guaranteeing the safety of the cell. Indeed, the peculiar morphology of the nanofibrous separators enhances the surface to volume ratio, promoting the interaction with the electrolyte. This also permits the easier movement of Li-ions towards electrodes, resulting in higher electrochemical performance.

In addition, since the thermal stability of the separators is one of the most significant indicators in the safety of LIBs, the thermo-mechanical shrinkage of the separator should be reduced to the minimum. If not, high temperatures will cause the positive and negative electrodes to directly contact, resulting in a short circuit, abrupt increase of temperature and, eventually, battery thermal runaway. On the contrary, nanofibrous mats may close their pores as the temperature increases beyond a given value, preventing the short circuit and the thermal runaway of the cell.

In this study, a methodology for enhancing nanofibrous membrane properties was presented through the incorporation of ZrO_2, SiO_2 and SnO_2 nanoparticles at varying concentrations into a polymeric solution. SEM and FTIR analyses confirmed the uniform morphology and chemical structure of the resulting mats, while thermal and electrochemical characterisations provided insight into their performance. The incorporation of ZrO_2 and SnO_2 improved the tensile strength, while SiO_2 enhanced elongation at lower concentrations. The elastic modulus increased with nanofiller content, reaching a maximum of ~240 MPa for the mat containing 7 wt% ZrO_2. Thermal shrinkage tests demonstrated superior thermal stability for the ZrO_2-filled mats, with a 75% shrinkage reduction at high temperatures compared to the neat separator. Although electrolyte uptake slightly decreased upon nanoparticle addition, the values remained acceptable, particularly for the SiO_2-filled membranes. Electrochemical impedance spectroscopy revealed that ZrO_2-filled separators had the lowest internal resistance, indicating improved ionic transport properties.

Finally, battery cycling tests demonstrated that cells with nanofibrous separators had higher specific capacities at lower C-rates compared to commercial Celgard separators. Overall, the material that exhibited the best performance across various C-rates was the one filled with 7 wt% of Zirconia. Nonetheless, high C-rates (> 0.5C) causes a significant drop in the specific capacity, particularly in cells with SiO_2-filled separators, highlighting the limitations of ion migration in these configurations.

All this being highlighted, it may be concluded that, among the nanofillers used in this work, ZrO_2-filled PVDF-HFP separators offer the best balance of mechanical strength, thermal stability, and electrochemical performance, making them promising

25143255, 2025, 1, Downloaded from https://ietresearch.onlinelibrary.wiley.com/doi/10.1049/ndc2.70021 by Area Sistemi Dipart & Doc, Wiley Online Library on [31/10/2025]. See the Terms and Conditions (https://onlinelibrary.wiley.com/terms-and-conditions) on Wiley Online Library for rules of use; OA articles are governed by the applicable Creative Commons License

candidates for advanced LIBs. In particular, the separator with 7 wt% of ZrO_2 has the best performance in terms of shrinkage percentage, elastic modulus and specific capacity under cycling tests, while the other properties remain quite stable if compared to the neat sample. This material is, thus, suggested as a valid alternative to the commercial Celgard separators for Li-ion batteries thanks to the improved mechanical and thermal stability, along with electrochemical properties.

Future works on this topic will include the study of coin-cell batteries employing more efficient active materials (e.g., high performance transition metal oxides cathodes) to achieve performance typical of traditional coin cell batteries. Moreover, on the most promising separator that is, nanofibrous mat with 7 wt% ZrO_2, an aging campaign on the full cell is planned, including life cycling to 80% depth of discharge (DoD).

Author Contributions

Leonardo Gasperini: conceptualization, data curation, formal analysis, investigation, methodology, writing – original draft. **Iacopo Iannarelli:** data curation, formal analysis, investigation. **Simone Vincenzo Suraci:** conceptualization, data curation, methodology, writing – review and editing. **Davide Fabiani:** conceptualization, supervision, writing – review and editing.

Acknowledgements

Open access publishing facilitated by Universita degli Studi di Bologna, as part of the Wiley - CRUI-CARE agreement.

Conflicts of Interest

The authors declare no conflicts of interest.

Data Availability Statement

Data available on request from the authors.

References

1. J. C. Barbosa, R. Gonçalves, C. M. Costa, and S. Lanceros-Mendez, "Recent Advances on Materials for Lithium-Ion Batteries," *Energies* 14, no. 11 (2021): 3145, https://doi.org/10.3390/en14113145.

2. H. Cheng, J. G. Shapter, Y. Li, and G. Gao, "Recent Progress of Advanced Anode Materials of Lithium-Ion Batteries," *Journal of Energy Chemistry* 57 (2021): 451–468, https://doi.org/10.1016/j.jechem.2020.08.056.

3. G. Selleri, F. Poli, R. Neri, et al., "Energy Harvesting and Storage With Ceramic Piezoelectric Transducers Coupled With an Ionic Liquid-Based Supercapacitor," *Journal of Energy Storage* 60, no. November 2022 (2023): 106660, https://doi.org/10.1016/j.est.2023.106660.

4. F. Tang, Y. Tan, T. Jiang, and Y. Zhou, "Phosphorus-Doped Silicon Nanoparticles as High Performance LIB Negative Electrode," *Journal of Materials Science* 57, no. 4 (2022): 2803–2812, https://doi.org/10.1007/s10853-021-06679-3.

5. Y. He, H. Xu, F. Liu, et al., "Structural Evolution of Dendritic-Structured Mg0.01V2O5 Film Electrodes of Lithium-Ion Batteries During Cycling," *Electrochimica Acta* 446, no. February (2023): 142078, https://doi.org/10.1016/j.electacta.2023.142078.

6. J. Zheng, G. Xing, L. Jin, et al., "Strategies and Challenge of Thick Electrodes for Energy Storage: A Review," *Batteries* 9, no. 3 (2023): 151, https://doi.org/10.3390/batteries9030151.

7. Z. Zheng, Z. Ju, S. Ma, et al., "Napthalene Diimide Derivative Based Organic Cocrystal Frameworks as Cathode Electrodes for Stable Lithium Batteries," *New Journal of Chemistry* 47, no. 16 (2023): 7476–7480, https://doi.org/10.1039/d3nj00698k.

8. J. L. Pan, Z. Zhang, H. Zhang, et al., "Ultrathin and Strong Electrospun Porous Fiber Separator," *ACS Applied Energy Materials* 1, no. 9 (2018): 4794–4803, https://doi.org/10.1021/acsaem.8b00855.

9. R. B. MacMullin and G. A. Muccini, "Characteristics of Porous Beds and Structures," *AIChE Journal* 2, no. 3 (1956): 393–403, https://doi.org/10.1002/aic.690020320.

10. P. Arora and Z. Zhang, "Battery Separators," *Chemical Reviews* 104, no. 10 (2004): 4419–4462, https://doi.org/10.1021/cr020738u.

11. M. Makki, C. W. Lee, and G. Ayoub, "Stress Distribution Inside a Lithium-Ion Battery Cell During Fast Charging and Its Effect on Degradation of Separator," *Batteries* 9, no. 10 (2023): 502, https://doi.org/10.3390/batteries9100502.

12. H. Li, D. Zhou, J. Cao, Z. Li, and C. Zhang, "On the Damage and Performance Degradation of Multifunctional Sandwich Structure Embedded With Lithium-Ion Batteries Under Impact Loading," *Journal of Power Sources* 581, no. August (2023): 233509, https://doi.org/10.1016/j.jpowsour.2023.233509.

13. W. Xiao, K. Zhang, J. Liu, and C. Yan, "Preparation of Poly(vinyl alcohol)-Based Separator With Pore-Forming Additive for Lithium-Ion Batteries," *Journal of Materials Science: Materials in Electronics* 28, no. 23 (2017): 17516–17525, https://doi.org/10.1007/s10854-017-7687-7.

14. Y. Shi, B. Yuan, Y. He, et al., "Preparation of Porous Fluorinated Polyimide Separator for Lithium-Ion Batteries by Non-Solvent Induced Phase Separation Process," *High Performance Polymers* 33, no. 7 (2021): 774–784, https://doi.org/10.1177/0954008320988156.

15. J. P. Gu, K. Y. Zhang, X. T. Li, J. Dong, Q. H. Zhang, and X. Zhao, "Construction of Safety and Non-flammable Polyimide Separator Containing Carboxyl Groups for Advanced Fast Charing Lithium-Ion Batteries," *Chinese Journal of Polymer Science* 40, no. 4 (2022): 345–354, https://doi.org/10.1007/s10118-022-2678-4.

16. M. Palanisamy, K. W. Lin, C. T. Lo, and V. G. Pol, "In Situ Thermal Safety Aspect of the Electrospun Polyimide-Al2O3Separator Reveals Less Exothermic Heat Energies Than Polypropylene at the Thermal Runaway Event of Lithium-Ion Batteries," *ACS Applied Materials and Interfaces* 14, no. 24 (2022): 28310–28320, https://doi.org/10.1021/acsami.2c07780.

17. G. Zhu, X. Jing, D. Chen, and W. He, "Novel Composite Separator for High Power Density Lithium-Ion Battery," *International Journal of Hydrogen Energy* 45, no. 4 (2020): 2917–2924, https://doi.org/10.1016/j.ijhydene.2019.11.125.

18. Y. Ma, J. Hu, Z. Wang, Y. Zhu, X. Ma, and C. Cao, "Poly(vinylidene fluoride)/SiO2 Composite Membrane Separators for High-Performance Lithium-Ion Batteries to Provide Battery Capacity With Improved Separator Properties," *Journal of Power Sources* 451, no. January (2020): 227759, https://doi.org/10.1016/j.jpowsour.2020.227759.

19. A. Valverde, R. Gonçalves, M. M. Silva, et al., "Metal-Organic Framework Based PVDF Separators for High Rate Cycling Lithium-Ion Batteries," *ACS Applied Energy Materials* 3, no. 12 (2020): 11907–11919, https://doi.org/10.1021/acsaem.0c02044.

20. X. Zhang, X. Wang, H. Tang, and H. Shi, "PVDF-HFP/SiO2 Composite Solid Electrolyte Enhanced by Supramolecular Self-Assembly of Cyclodextrin," *Journal of Energy Storage* 88, no. January (2024): 111461, https://doi.org/10.1016/j.est.2024.111461.

21. K. W. Lee, S. M. Yeh, K. H. Ni, and C. C. Li, "Enhancing Electrochemical Performance of Solid-State Li-Ion Batteries With Composite Electrolytes of Fibrous LLZTO and PVDF-HFP: The Role of LLZTO Fiber Diameter," *Journal of Energy Storage* 74, no. PB (2023): 109531, https://doi.org/10.1016/j.est.2023.109531.

25143255, 2025, 1, Downloaded from https://ietresearch.onlinelibrary.wiley.com/doi/10.1049/ndc2.70021 by Area Sistemi Dipart & Doc, Wiley Online Library on [31/10/2025]. See the Terms and Conditions (https://onlinelibrary.wiley.com/terms-and-conditions) on Wiley Online Library for rules of use; OA articles are governed by the applicable Creative Commons License

22. A. Das, A. Melepurakkal, P. Sreeram, et al., "Exceptional Cyclability of Thermally Stable PVdF-co-HFP/SiO2 Nanocomposite Polymer Electrolytes for Sodium Ion Batteries," *Journal of Energy Storage* 73, no. PC (2023): 109026, https://doi.org/10.1016/j.est.2023.109026.

23. B. Wang and H. X. Huang, "Incorporation of Halloysite Nanotubes Into PVDF Matrix: Nucleation of Electroactive Phase Accompany With Significant Reinforcement and Dimensional Stability Improvement," *Composites Part A: Applied Science and Manufacturing* 66 (2014): 16–24, https://doi.org/10.1016/j.compositesa.2014.07.001.

24. C. M. Costa, M. M. Silva, and S. Lanceros-Méndez, "Battery Separators Based on Vinylidene Fluoride (VDF) Polymers and Copolymers for Lithium Ion Battery Applications," *RSC Advances* 3, no. 29 (2013): 11404–11417, https://doi.org/10.1039/c3ra40732b.

25. C. M. Costa and S. Lanceros-Mendez, "Recent Advances on Battery Separators Based on Poly(vinylidene fluoride) and Its Copolymers for Lithium-Ion Battery Applications," *Current Opinion in Electrochemistry* 29 (2021): 100752, https://doi.org/10.1016/j.coelec.2021.100752.

26. N. A. Kyeremateng, D. Gukte, M. Ferch, J. Buk, T. Hrebicek, and R. Hahn, "Preparation of a Self-Supported SiO2 Membrane as a Separator for Lithium-Ion Batteries," *Batteries & Supercaps* 3, no. 5 (2020): 456–462, https://doi.org/10.1002/batt.201900169.

27. J. C. Barbosa, D. M. Correia, R. Gonçalves, et al., "Enhanced Ionic Conductivity in Poly(vinylidene fluoride) Electrospun Separator Membranes Blended With Different Ionic Liquids for Lithium Ion Batteries," *Journal of Colloid and Interface Science* 582, no. Pt A (2021): 376–386, https://doi.org/10.1016/j.jcis.2020.08.046.

28. M. Cai, D. Yuan, X. Zhang, et al., "Lithium Ion Battery Separator With Improved Performance via Side-by-Side Bicomponent Electrospinning of PVDF-HFP/PI Followed by 3D Thermal Crosslinking," *Journal of Power Sources* 461, no. September 2019 (2020): 1–10, https://doi.org/10.1016/j.jpowsour.2020.228123.

29. C. Zhang, V. S. Reddy, and S. Ramakrishna, "Advancing Lithium-Ion Battery Technology With Electrospun PVDF-HFP/SiO2 Nanocomposite Electrolyte Membrane and CuCo2O4 High-Performance Anode Material," *Journal of Energy Storage* 87, no. December 2023 (2024): 111429, https://doi.org/10.1016/j.est.2024.111429.

30. M. Khalifa, S. Janakiraman, R. Biswal, S. Ghosh, V. Adyam, and S. Anandhan, "Design and Development of a High-Performance Gel Polymer Electrolyte for Na-Ion Battery From Halloysite Nanotube-Dispersed PVDF Nanofabrics," *ACS Applied Engineering Materials* 3, no. 7 (2025): 2020–2030, https://doi.org/10.1021/acsaenm.5c00199.

31. C. Shamitha, S. Janakiraman, S. Ghosh, A. Venimadhav, K. N. Prabhu, and S. Anandhan, "Synthesis and Evaluation of a New Gel Polymer Electrolyte for High-Performance Li-Ion Batteries From Electrospun Nanocomposite of PVDF/Ca–Al-Layered Double Hydroxide," *Journal of Materials Research* 37, no. 22 (2022): 3942–3954, https://doi.org/10.1557/s43578-022-00700-4.

32. M. Chen, W. Liu, Y. Wu, Y. Liu, Y. Wang, and Z. Chen, "Li6.25Al0.25La3Zr1.75Nb0.25O12 Nanofiber Fillers Reinforced PVDF-HFP-Based Bilayer Composite Solid-State Electrolytes," *Batteries & Supercaps* 8, no. 2 (2024): 202400379, https://doi.org/10.1002/batt.202400379.

33. J. K. Kim, G. Cheruvally, X. Li, J. H. Ahn, K. W. Kim, and H. J. Ahn, "Preparation and Electrochemical Characterization of Electrospun, Microporous Membrane-Based Composite Polymer Electrolytes for Lithium Batteries," *Journal of Power Sources* 178, no. 2 (2008): 815–820, https://doi.org/10.1016/j.jpowsour.2007.08.063.

34. P. Raghavan, J. W. Choi, J. H. Ahn, et al., "Novel Electrospun Poly (vinylidene fluoride-co-hexafluoropropylene)-In Situ SiO2 Composite Membrane-Based Polymer Electrolyte for Lithium Batteries," *Journal of Power Sources* 184, no. 2 (2008): 437–443, https://doi.org/10.1016/j.jpowsour.2008.03.027.

35. P. Raghavan, X. Zhao, J. K. Kim, et al., "Ionic Conductivity and Electrochemical Properties of Nanocomposite Polymer Electrolytes Based on Electrospun Poly(vinylidene fluoride-co-hexafluoropropylene) With Nano-Sized Ceramic Fillers," *Electrochimica Acta* 54, no. 2 (2008): 228–234, https://doi.org/10.1016/j.electacta.2008.08.007.

36. S. Jia, J. Long, J. Li, et al., "Biomineralized Zircon-Coated PVDF Nanofiber Separator for Enhancing Thermo- and Electro-Chemical Properties of Lithium Ion Batteries," *Journal of Materials Science* 55, no. 30 (2020): 14907–14921, https://doi.org/10.1007/s10853-020-05051-1.

37. L. Gasperini, S. Gandolfi, S. V. Suraci, and D. Fabiani, "Electrical and Mechanical Properties of Electrospun PVDF-HFP With ZrO 2 Nanoparticles Used as Separator in Electrochemical Systems," in *2023 IEEE Conf Electr Insul Dielectr Phenom* (2023), 1–4, https://doi.org/10.1109/CEIDP51414.2023.10410461.

38. A. K. Solarajan, V. Murugadoss, and S. Angaiah, "Dimensional Stability and Electrochemical Behaviour of ZrO 2 Incorporated Electrospun PVdF-HFP Based Nanocomposite Polymer Membrane Electrolyte for Li-Ion Capacitors," *Scientific Reports* 7, no. February (2017): 1–10, https://doi.org/10.1038/srep45390.

39. D. Wu, L. Deng, Y. Sun, et al., "A High-Safety PVDF/Al2O3 Composite Separator for Li-Ion Batteries via Tip-Induced Electrospinning and Dip-Coating," *RSC Advances* 7, no. 39 (2017): 24410–24416, https://doi.org/10.1039/c7ra02681a.

40. L. Wang, C. Li, J. Zhang, et al., "The Electrical Conductivity and Mechanical Properties of Monolayer and Multilayer Nanofibre Membranes From Different Fillers: Calculated Based on Parallel Circuit," *Polymers (Basel)* 14, no. 22 (2022): 5048, https://doi.org/10.3390/polym14225048.

41. E. Maccaferri, L. Mazzocchetti, T. Benelli, T. M. Brugo, A. Zucchelli, and L. Giorgini, "Rubbery Nanofibers by Co-Electrospinning of Almost Immiscible NBR and PCL Blends," *Materials and Design* 186 (2020): 108210, https://doi.org/10.1016/j.matdes.2019.108210.

42. A. Terella, F. De Giorgio, M. Rahmanipour, et al., "Functional Separators for the Batteries of the Future," *Journal of Power Sources* 449, no. November 2019 (2020): 227556, https://doi.org/10.1016/j.jpowsour.2019.227556.

43. S. Ramesh, S. C. Lu, and I. Vankelecom, "BMIMTf Ionic Liquid-Assisted Ionic Dissociation of MgTf in P(VdF-HFP)-Based Solid Polymer Electrolytes," *Journal of Physics and Chemistry of Solids* 74, no. 10 (2013): 1380–1386, https://doi.org/10.1016/j.jpcs.2013.04.017.

44. V. Aravindan, P. Vickraman, and T. P. Kumar, "Polyvinylidene Fluoride-Hexafluoropropylene (PVdF-HFP)-Based Composite Polymer Electrolyte Containing LiPF3(CF3CF2)3," *Journal of Non-Crystalline Solids* 354, no. 29 (2008): 3451–3457, https://doi.org/10.1016/j.jnoncrysol.2008.03.009.

45. R. Gregorio and M. Cestari, "Effect of Crystallization Temperature on the Crystalline Phase Content and Morphology of Poly(vinylidene fluoride)," *Journal of Polymer Science Part B: Polymer Physics* 32, no. 5 (1994): 859–870, https://doi.org/10.1002/polb.1994.090320509.

46. D. Mandal, K. Henkel, and D. Schmeißer, "Improved Performance of a Polymer Nanogenerator Based on Silver Nanoparticles Doped Electrospun P(VDF-HFP) Nanofibers," *Physical Chemistry Chemical Physics* 16, no. 22 (2014): 10403–10407, https://doi.org/10.1039/c3cp55238a.

47. M. M. Rashad and H. M. Baioumy, "Effect of Thermal Treatment on the Crystal Structure and Morphology of Zirconia Nanopowders Produced by Three Different Routes," *Journal of Materials Processing Technology* 195, no. 1–3 (2008): 178–185, https://doi.org/10.1016/j.jmatprotec.2007.04.135.

48. B. Zhang, Y. Tian, J. X. Zhang, and W. Cai, "The FTIR Studies of SnO2: Sb(ATO) Films Deposited by Spray Pyrolysis," *Materials Letters* 65, no. 8 (2011): 1204–1206, https://doi.org/10.1016/j.matlet.2011.01.052.

25143255, 2025, 1, Downloaded from https://ietresearch.onlinelibrary.wiley.com/doi/10.1049/ndi2.70021 by Area Sistemi Dipart & Doc, Wiley Online Library on [31/10/2025]. See the Terms and Conditions (https://onlinelibrary.wiley.com/terms-and-conditions) on Wiley Online Library for rules of use; OA articles are governed by the applicable Creative Commons License

49. Q. Hu, H. Suzuki, H. Gao, H. Araki, W. Yang, and T. Noda, "High-Frequency FTIR Absorption of SiO2/Si Nanowires," *Chemical Physics Letters* 378, no. 3–4 (2003): 299–304, https://doi.org/10.1016/j.cplett.2003.07.015.

50. D. Parikh, T. Christensen, C. T. Hsieh, and J. Li, "Elucidation of Separator Effect on Energy Density of Li-Ion Batteries," *Journal of the Electrochemical Society* 166, no. 14 (2019): A3377–A3383, https://doi.org/10.1149/2.0571914jes.

25143255, 2025, 1, Downloaded from https://ietresearch.onlinelibrary.wiley.com/doi/10.1049/ndd2.70021 by Area Sistemi Dipart & Doc, Wiley Online Library on [31/10/2025]. See the Terms and Conditions (https://onlinelibrary.wiley.com/terms-and-conditions) on Wiley Online Library for rules of use; OA articles are governed by the applicable Creative Commons License